

Idealized Particle-Resolved Large-Eddy Simulations to Evaluate the Impact of Emissions Spatial Heterogeneity on CCN Activity

Samuel G. Frederick¹, Matin Mohebalhojeh², Jeffrey H. Curtis^{1,2}, Matthew West², and Nicole Riemer¹

¹Department of Climate, Meteorology, and Atmospheric Sciences, University of Illinois Urbana–Champaign, 1301 W. Green St., Urbana, IL 61801, USA

²Department of Mechanical Science and Engineering, University of Illinois Urbana–Champaign, 1206 W. Green St., Urbana, IL, 61801, USA

Correspondence: Samuel G. Frederick (sf20@illinois.edu) and Nicole Riemer (nriemer@illinois.edu)

Abstract. Aerosol-cloud interactions remain a large source of uncertainty in global climate models (GCMs) due to complex, non-linear processes that alter aerosol properties and the inability to represent the full compositional complexity of aerosol populations within large-scale modeling frameworks. The spatial resolution of GCMs is often coarser than the scale of the spatially varying emissions in the modeled geographic region. This results in diffuse, uniform concentration fields of primary aerosol 5 and gas-phase species instead of spatially heterogeneous concentrations. Aerosol processes such as gas-particle partitioning and coagulation are concentration-dependent in a non-linear manner, and thus the representation of spatially heterogeneous emissions impacts aerosol aging and properties. This includes climate-relevant quantities key to aerosol-cloud interactions including particle hygroscopicity and cloud condensation nuclei (CCN) activity. We investigate the impact of emissions spatial heterogeneity on aerosol properties including CCN activity via a series of first-of-a-kind particle-resolved large-eddy simulations 10 with the modeling framework WRF-PartMC-MOSAIC-LES. CCN concentrations within the planetary boundary layer (PBL) are compared across numerous scenarios ranging in emissions spatial heterogeneity. CCN concentrations at low supersaturations ($S_{\text{env}} = 0.1\text{--}0.3\%$) increase in the upper PBL by up to 25% for emissions scenarios with high spatial heterogeneity when compared to a uniform emissions base case. Process level analysis indicates that this increase is due to enhanced nitrate formation among scenarios with high emissions spatial heterogeneity.

15 1 Introduction

Aerosols exert a net negative radiative forcing, but significant uncertainty remains in how aerosol-cloud interactions are represented in climate models (Forster et al., 2021). Two major factors contribute to this uncertainty: (1) the spatial resolution of models and (2) the treatment of aerosol representation, which refers to how aerosol properties such as size distribution, chemical composition, and mixing state are modeled.

20 Advances in computational power have allowed modelers to investigate how spatial resolution affects radiative forcing due to aerosol-cloud interactions (Ma et al., 2015). At the same time, increasing computational capabilities have enabled more sophisticated aerosol representations (Zaveri et al., 2021; Tilmes et al., 2023). While both spatial resolution and aerosol representation have advanced, they have largely been studied in isolation. The combined effect of sub-grid scale spatial heterogeneity

and detailed aerosol representation on relevant properties, such as cloud condensation nuclei (CCN) activity, remains largely unexplored. The goal of this paper is to investigate their combined impact on key microphysical properties, with a focus on cloud condensation nuclei (CCN) activity.

Aerosol-aware climate models typically include a sub-model that governs aerosol representation and associated processes. Due to computational constraints, these aerosol treatments often simplify compositional diversity. For instance, the Energy Exascale Earth System Model (E3SM) uses the MAM4 scheme, which represents aerosols using four internally mixed, log-normally distributed modes (Golaz et al., 2022). This approach inherently constrains the diversity of aerosol populations, as all particles within a given mode share identical composition. In reality, however, aerosols age independently, leading to complex, highly heterogeneous mixtures. Particle-resolved aerosol models address this limitation by explicitly tracking the composition and evolution of individual particles. The Particle Monte Carlo model (PartMC) (Riemer et al., 2009) has been extensively used to study the sensitivity of CCN activity to aerosol composition (Fierce et al., 2013), aging timescales due to condensation and coagulation for carbonaceous CCN (Fierce et al., 2015), and the impact of mixing state on CCN estimates (Ching et al., 2017). Furthermore, PartMC has been leveraged to quantify errors in CCN predictions from modal and sectional models by comparing CCN concentrations against those derived from fully resolved aerosol compositions (Zaveri et al., 2010; Ching et al., 2017). Comparisons between PartMC and MAM4 have revealed substantial discrepancies in CCN activity, particularly in polluted regions where coagulation and gas-particle partitioning amplify model differences (Fierce et al., 2024).

Despite these advancements in aerosol representation, a critical gap remains: the combined effects of high-resolution aerosol treatment and fine-scale spatial heterogeneity have yet to be systematically explored. Understanding this interaction is essential, as the variability in surface properties, emissions, and resulting aerosol plumes influences particle aging and CCN activity. The goal of this study is to bridge this gap by conducting the first particle-resolved large-eddy simulations (LES) to analyze how sub-grid scale spatial heterogeneity affects aerosol composition, aging, and CCN activation.

Existing regional and global-scale aerosol-aware models lack the resolution to fully capture fine-scale spatial heterogeneities, leading to artificially uniform concentrations within grid cells. This oversimplification distorts the representation of non-linear aerosol processes such as coagulation and gas-particle partitioning. Studies have demonstrated that climate-relevant aerosol properties, including aerosol optical properties (Gustafson Jr. et al., 2011) and CCN activity (Weigum et al., 2016), are highly sensitive to model resolution. Much of the sub-grid scale variability arises from spatially heterogeneous emissions (Qian et al., 2010), yet many climate models fail to resolve this variability adequately.

Prior research on sub-grid variability of aerosol properties has typically compared coarse-resolution global climate models (50–100 km) against higher-resolution simulations (1–10 km) (Qian et al., 2010; Gustafson Jr. et al., 2011; Weigum et al., 2016; Crippa et al., 2017; Lin et al., 2017). While increasing model resolution improves the representation of emissions heterogeneities, unresolved spatial variability persists at sub-kilometer scales. Additionally, climate models rely on Reynolds-averaged Navier-Stokes parameterizations to represent boundary-layer turbulence, which fail to capture the full complexity of turbulent transport and its influence on aerosol processes.

Another approach to investigating sub-grid heterogeneity has been to use LES, which explicitly captures fine-scale turbulent mixing and chemical segregation. Brasseur et al. (2023) review LES applications investigating turbulence-chemistry interac-

tions in spatially heterogeneous environments. Many LES studies have focused on gas-phase chemistry, particularly the oxidation of reactive volatile organic compounds (VOCs) such as isoprene, demonstrating that spatially heterogeneous emissions contribute to chemical segregation between reactive species in the boundary layer (Ouwersloot et al., 2011; Kaser et al., 2015). Given the coupling between gas and aerosol phases through gas-particle partitioning, it is likely that chemical segregation due to spatially heterogeneous emissions also influences aerosol properties. While some LES-based studies have incorporated aerosols, they have largely relied on simplified treatments. Recent efforts have coupled turbulence-resolving frameworks with aerosol models, such as the Sectional Aerosol Model for Large Scale Applications (SALSA) (Kokkola et al., 2008) with UCLALES (Tonttila et al., 2017) as well as the Parallelized Large-Eddy Simulation Model (PALM) (Kurppa et al., 2019). Additional efforts coupling LES with prognostic aerosol treatments include the modal aerosol model M7 (Vignati et al., 2004) with the Dutch Atmospheric Large-Eddy Simulation model (DALES) (de Bruine et al., 2019). However, despite their high-resolution transport schemes, these models rely on relatively coarse aerosol representations. For example, UCLALES-SALSA employs a 10-bin sectional scheme, while DALES modifies the seven-mode M7 model to incorporate additional hydrometeor modes. To our knowledge, no turbulence-resolving model has yet incorporated a particle-resolved aerosol treatment, which would enable a fully detailed representation of aerosol composition, properties, and aging alongside LES-resolved turbulent transport.

This study aims to analyze the coupled effects of spatial heterogeneity in surface emissions (including both gas-phase species and primary aerosols), aerosol aging processes, and their impact on CCN activity. To achieve this, we conduct the first particle-resolved LES simulations, establishing a high-resolution aerosol-transport modeling framework that explicitly represents both turbulent transport and aerosol composition.

This paper is organized in the following manner. Section 2 presents the modeling framework, WRF-PartMC-MOSAIC-LES, along with a description of emissions scenarios with varying spatial heterogeneity. Section 3 discusses the results of simulation runs, including changes in aerosol size distribution, composition, hygroscopicity, and CCN activity. We conclude with remarks on the implications of this study, limitations stemming from its idealized nature, and potential directions for future work.

2 Methods

2.1 WRF-PartMC-MOSAIC-LES

The aerosol-transport model WRF-PartMC-MOSAIC-LES integrates multiple sub-models responsible for transport, aerosol representation, and multiphase chemistry. It extends the aerosol-transport column model WRF-PartMC, originally developed by Curtis et al. (2017) and later extended to include advection (Curtis et al., 2024). WRF-PartMC couples the Weather Research and Forecasting model (WRF) (Skamarock et al., 2008) with the particle-resolved aerosol model PartMC (Riemer et al., 2009). PartMC represents a population of aerosol particles using an ensemble of computational particles, each assigned a weight (i.e., particle multiplicity) to capture the diversity of particle sizes and composition observed in real-world aerosol populations. As particles age, their composition evolves dynamically. Since PartMC operates as a box model it does not track the spatial position of individual particles within a computational grid cell. Instead, particle transport is handled by a stochastic advection

algorithm that interfaces with WRF's dynamical core (Curtis et al., 2024). WRF-PartMC has been used in one-dimensional simulations to resolve vertical gradients in aerosol composition and mixing state (Curtis et al., 2017) and, more recently, in three-dimensional simulations to study aerosol transport within a regional domain driven by simulated meteorology (Curtis et al., 2024).

LES models explicitly resolve large-scale turbulent motion, typically at the scale of 10–100 m; however, they must parameterize sub-grid scale eddies and the down-gradient tendency of turbulent kinetic energy (TKE) as it propagates from large to small scales, where it ultimately dissipates as heat. This requires the use of closure schemes. In WRF-PartMC-MOSAIC-LES, turbulent mixing is parameterized using Deardorff's TKE scheme for eddy diffusivity and eddy viscosity (Deardorff, 1980).

Gas-phase chemistry, gas-aerosol partitioning, and aerosol thermodynamics are represented using the Model for Simulating Aerosol Interactions and Chemistry (MOSAIC) (Zaveri et al., 2008). MOSAIC is comprised of multiple sub-models, including the Carbon Bond Mechanism version Z (CBM-Z) which solves gas phase chemistry (Zaveri and Peters, 1999). Phase-dependent partitioning of aerosol species is handled by the Multicomponent Equilibrium Solver for Aerosols (MESA) (Zaveri et al., 2005a). Activity coefficients of electrolytes are parameterized via the Multicomponent Taylor Expansion Method (MTEM) (Zaveri et al., 2005b). To efficiently solve the numerically stiff set of solid-liquid phase reactions, MOSAIC employs the Adaptive Step Time-Split Euler Method (ASTEM) (Zaveri et al., 2008). MOSAIC models aerosol chemistry for both inorganic and organic compounds such as nitrate, ammonium, sulfate, black carbon (BC), and a limited set of secondary organic aerosol (SOA) species.

2.2 Computational domain setup

The computational domain extends 10 km in both the x - and y -directions, with a horizontal grid spacing of 100 m. Vertically, the domain reaches 2 km and is represented with 200 vertical levels. LES runs in WRF use an η vertical coordinate system, whereby vertical levels are linearly spaced in pressure. Due to the limited depth of the domain, this results in an effective vertical resolution of approximately 10 m. Simulations begin on the Vernal Equinox at 09:00 local time (LT) and conclude at 15:00 LT for a total duration of 6 hours to maintain balanced photolysis rates throughout the simulation period. Each grid cell is initialized with 100 computational particles, resulting in 100 million total particles. As processes such as emission, transport, and coagulation modify the number concentration of particles, the total number of computational particles within each grid cell is dynamically adjusted—doubling when it falls to half the initial value and halving when it reaches twice the initial value—to maintain computational efficiency and adequate representation of the aerosol state.

In particle-resolved box model studies, a typical choice is $N_p \sim 10,000$ computational particles to minimize stochastic variability in aerosol processes (Curtis et al., 2024; Liu et al., 2025). However, for three-dimensional large-eddy simulations (LES) coupled with PartMC, the computational burden scales with the number of grid cells, making such high particle counts per cell impractical. In this study, we used 100 particles per grid cell—a choice that balances computational cost and model fidelity. While lower N_p increases stochastic variability at the individual grid-cell level, our focus is on domain-scale patterns and contrasts driven by spatial heterogeneity, which are robust to such noise. Simulations were conducted on a high-performance

125 computing cluster using 384 CPU cores in parallel. Future studies may explore sensitivity to N_p , but we expect the main conclusions presented here to remain valid.

The domain is initialized over a flat, uniform land surface absent of topographic features or land-use variations. WRF-PartMC-MOSAIC-LES is not coupled to one of WRF's radiation sub-models. Instead, MOSAIC employs idealized parameterizations to determine photolysis rates based on the solar zenith angle. Due to the lack of a radiation sub-model, surface heating
130 is imposed uniformly across the domain using a constant rate of 0.24 K ms^{-1} , which is representative of typical kinematic heat fluxes observed during mid-day in clear sky conditions over land (Stull, 1988).

Initial conditions and emissions for both aerosols and the gas phase represent an urban environment and are based on Riemer et al. (2009). The initial concentrations and emission rates stem from the 1987 Southern California Air Quality Study (SCAQS), which collected measurements of gas phase species and particulate matter mass concentrations at multiple sites across the Los
135 Angeles basin (Zaveri et al., 2008). Table 1 provides initial concentrations and emission rates for gas phase species, while Table 2 details aerosol initial conditions and emission rates categorized by aerosol modes. Initially, the aerosol consists of an internal mixture composed of 50% ammonium sulfate and 50% primary organic aerosol (POA) by mass. The three emission modes representing cooking and vehicular combustion comprise varying mixtures of POA and BC. The three emission modes, representing cooking and vehicular combustion sources, each consist of distinct fixed mixtures of primary organic aerosol
140 (POA) and black carbon (BC). To allow for simulation spin-up and the full development of the convective boundary layer, emissions remain at zero during the first hour of simulation. Subsequently, surface emissions are released at constant rates as specified by Tables 1 and 2 for the remainder of simulations.

Meteorological initial conditions define an idealized convective boundary layer structure, where the surface is 5 K warmer than the mixing layer, and an inversion of 8 K caps the layer at 1 km. The wind profile is set to zero throughout the domain.

145 2.3 Emissions Scenarios

To assess the impact of emissions spatial heterogeneity on aerosol properties, we examine multiple emissions scenarios, shown in Figure 1. The first scenario distributes emissions evenly across the entire domain and thus has no spatial heterogeneity. This serves as a proxy for coarser-resolution models that do not resolve spatial heterogeneity of emissions and instead assume uniform emissions of gases and primary aerosols across grid cells. The remaining scenarios introduce increasing levels of spatial
150 heterogeneity, enabling direct comparison against the no heterogeneity scenario to evaluate an emission pattern's influence on aerosol properties. The low heterogeneity scenario represents an idealized urban-rural interface, where emissions are released in half the domain with no emissions occurring in the other half. The medium heterogeneity scenario contains a narrow strip of emissions running through the center of the domain, corresponding to an emission pattern typical of a major roadway. Lastly, in the high heterogeneity scenario, all emissions are placed in a single grid cell in the domain center representing a point source
155 such as an industrial plume.

Spatial heterogeneity is quantified using the metric η developed by (Mohebalhojeh et al., 2025). The metric η is a normalized measure of spatial heterogeneity, ranging from 0 (completely homogeneous) to 1 (maximally heterogeneous). For a discrete 2-dimensional scalar field f over a domain S with lateral dimensions N by M , η is defined as

Table 1. Gas phase emissions and initial conditions. Table adapted from Riemer et al. (2009) with permission.

Species	Symbol	Initial Mole Fraction (ppb)	Emissions (nmol m ⁻² s ⁻¹)
Nitric oxide	NO	0.1	31.8
Nitrogen dioxide	NO ₂	1.0	1.67
Nitric acid	HNO ₃	1.0	
Ozone	O ₃	50.0	
Hydrogen peroxide	H ₂ O ₂	1.1	
Carbon monoxide	CO	21	291.3
Sulfur dioxide	SO ₂	0.8	2.51
Ammonia	NH ₃	0.5	6.11
Hydrogen chloride	HCl	0.7	
Methane	CH ₄	2200	
Ethane	C ₂ H ₆	1.0	
Formaldehyde	HCHO	1.2	1.68
Methanol	CH ₃ OH	0.12	0.28
Methyl hydrogen peroxide	CH ₃ OOH	0.5	
Acetaldehyde	ALD2	1.0	0.68
Paraffin carbon	PAR	2.0	96
Acetone	AONE	1.0	1.23
Ethene	ETH	0.2	7.2
Terminal olefin carbons	OLET	2.3 · 10 ⁻²	2.42
Internal olefin carbons	OLEI	3.1 · 10 ⁻⁴	2.42
Toluene	TOL	0.1	4.04
Xylene	XYL	0.1	2.41
Lumped organic nitrate	ONIT	0.1	
Peroxyacetyl nitrate	PAN	0.8	
Higher organic acid	RCOOH	0.2	
Higher organic peroxide	ROOH	2.5 · 10 ⁻²	
Isoprene	ISOP	0.5	0.23
Alcohols	ANOL		3.45

$$\eta(f, S) = \frac{2 \sum_{\tilde{S} \in \mathbf{D}} |\bar{f}(S) - \bar{f}(\tilde{S})|}{MN \bar{f}(S) [3MN - M - N - 1]}, \quad (1)$$

Table 2. Aerosol emissions and initial conditions. Table adapted from Riemer et al. (2009) with permission.

Initial/Background	N (m^{-3})	D_{gn} (μm)	σ_g	Composition by Mass
Aitken Mode	$3.2 \cdot 10^9$	0.02	1.45	50% $(\text{NH}_4)_2\text{SO}_4$, 50% POA
Accumulation Mode	$2.9 \cdot 10^9$	0.116	1.65	50% $(\text{NH}_4)_2\text{SO}_4$, 50% POA
Emissions	E ($\text{m}^{-2} \text{s}^{-1}$)	D_{gn} (μm)	σ_g	Composition by Mass
Meat cooking	$9 \cdot 10^6$	0.086	1.9	100% POA
Diesel vehicles	$1.6 \cdot 10^8$	0.05	1.7	30% POA, 70% BC
Gasoline vehicles	$5 \cdot 10^7$	0.05	1.7	80% POA, 20% BC

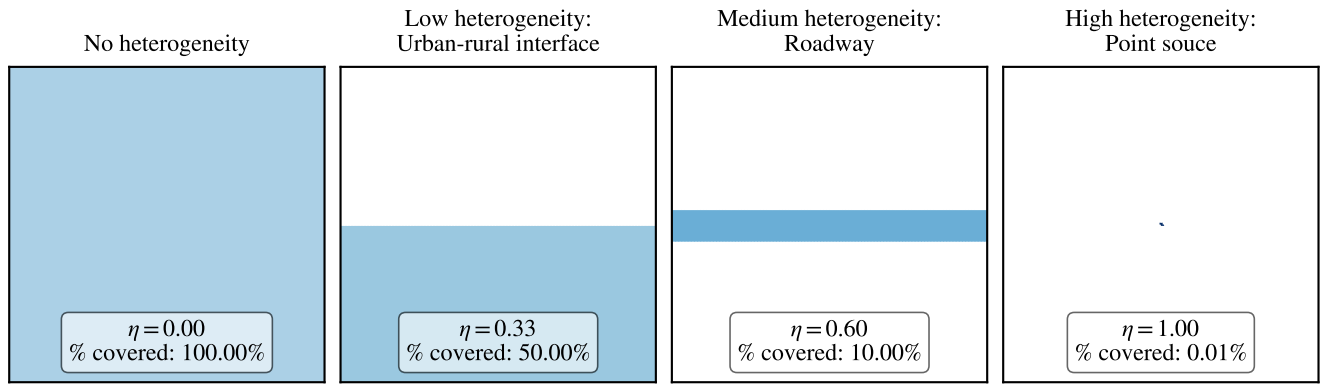


Figure 1. Emissions spatial heterogeneity scenarios. The pattern of emissions is shown as a cross section of the x - y plane at ground level. Shaded areas correspond to regions of emissions. The hue of shading indicates the intensity of emissions scaling ranging from light blue (low emissions scaling) to dark blue (high emissions scaling). Both the spatial heterogeneity metric η and the fraction of area covered by emissions are displayed in the bottom of each scenario.

160 where $\bar{f}(S)$ is the domain mean, $\bar{f}(\tilde{S})$ is the mean over a subset of the domain \tilde{S} , and \mathbf{D} is the set of all possible subdomains. Thus, the metric is computed by averaging the absolute value of the difference between the domain mean $\bar{f}(S)$ and all domain subset means $\bar{f}(\tilde{S})$, normalized by the maximum possible value of this average difference given a fixed domain mean. Mohebalhojeh et al. (2025) show that the metric is translationally invariant when the scalar field f is shifted within S . Furthermore, they prove that the maximum spatial heterogeneity occurs when the scalar field is zero everywhere except at a single point where it takes the value $MN \times \bar{f}(S)$.

The no heterogeneity scenario corresponds to the homogeneous condition ($\eta = 0$) while the high heterogeneity scenario—the point-source emission—represents the maximally heterogeneous case ($\eta = 1$). To ensure consistent mass emissions across

scenarios, emission rates are scaled by the fraction of area covered by emissions. For instance, in the high heterogeneity scenario, this results in a scaling of 10,000 ($M = N = 100$) for the point-source emission. The fraction of area covered by
170 emissions is displayed for each scenario alongside the spatial heterogeneity values in Figure 1.

3 Results

Key findings of this paper are structured as follows. Section 3.1 investigates the relationship between emissions spatial heterogeneity and the gas phase. Section 3.2 presents impacts of emissions spatial heterogeneity on bulk aerosol properties (number and mass concentrations). Section 3.3 discusses impacts on aerosol composition, with particular focus on sulfate, ammonium,
175 and nitrate due to their important role in particle hygroscopicity. Leveraging the particle-resolved framework, we further evaluate how particle hygroscopicity responds to emissions spatial heterogeneity. Building on these results, Section 3.4 investigates how emissions spatial heterogeneity impacts CCN activity across a range of supersaturation levels ranging (0.1% to 1.0%). Lastly, we explore the governing role of aerosol composition—namely, the presence of ammonia—in mediating the impact of emissions spatial heterogeneity on CCN activity.

180 3.1 Impacts of emissions spatial heterogeneity on gas phase species

Figure 2 displays x - y cross sections of ammonia, nitric acid, and the hydroxyl radical (OH) at $t = 6$ h taken at $z \approx 900$ m in the upper boundary layer. Among the three species, ammonia exhibits the highest spatial heterogeneity with η values 3–4 times higher than those of nitric acid and OH. This is primarily because ammonia is emitted while nitric acid and OH are formed due to chemical reactions. This leads to a marked concentration gradient for ammonia between regions near the emissions plume
185 (in excess of 10 ppbv directly over the emissions plume in the high heterogeneity scenario) and farther toward the perimeter of the domain (as low as 0.1 pptv).

Both OH and nitric acid exhibit much lower spatial heterogeneity due to a coupling between chemistry and the heterogeneity of each compound; however, the chemical mechanism underlying this coupling differs significantly between OH and nitric acid.
190 OH facilitates rapid oxidation of numerous compounds in the core of the emissions plume. While the concentration of OH is momentarily lowered due to oxidation reactions, it is quickly replenished via photolysis. As a result, local concentrations of OH are in near chemical-equilibrium as it is produced and consumed over very short timescales, preventing large scale spatial heterogeneity in the domain-wide concentration of OH. Whereas the concentration of OH is rapidly modified by oxidation and photolysis reactions in the gas phase, nitric acid is governed by equilibrium partitioning between the gas and aerosol phase. For instance, a nitrate rich particle which enters a parcel of air containing low levels of nitric acid will partition most of the nitrate
195 into the gas phase to re-establish thermodynamic equilibrium. Conversely, when the gas phase concentration nitric acid is high such as near an emissions plume, nitrate formation is favored. As a result, the reversible nature of ammonium nitrate formation acts as a buffer, regulating the concentration of nitric acid in the gas phase which lowers the degree of spatial heterogeneity.

Figure 3 presents vertical profiles of ammonia, nitric acid, and OH. For ammonia and nitric acid, the profiles show horizontal averages at each vertical level across the entire domain. As emissions spatial heterogeneity increases, both ammonia and nitric

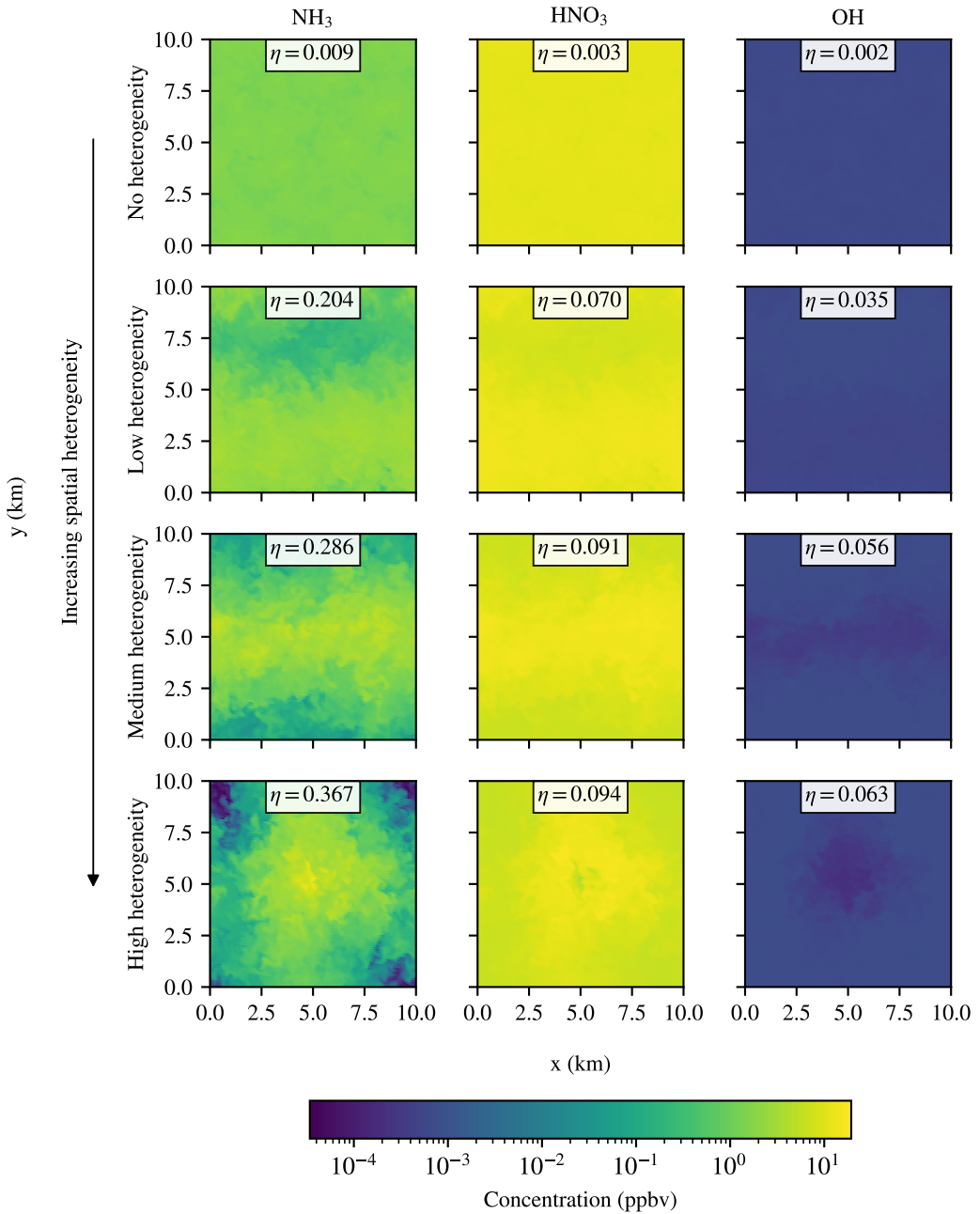


Figure 2. Cross sections in the x - y plane of gas phase species NH_3 (left column), HNO_3 (center column), and OH (right column). Cross sections are shown at a height of approximately $z \approx 900$ m and at $t = 6$ h. Coloring indicates the mixing ratio of gas species in parts per billion by volume. The value of the spatial heterogeneity metric η is displayed alongside each cross section plot.

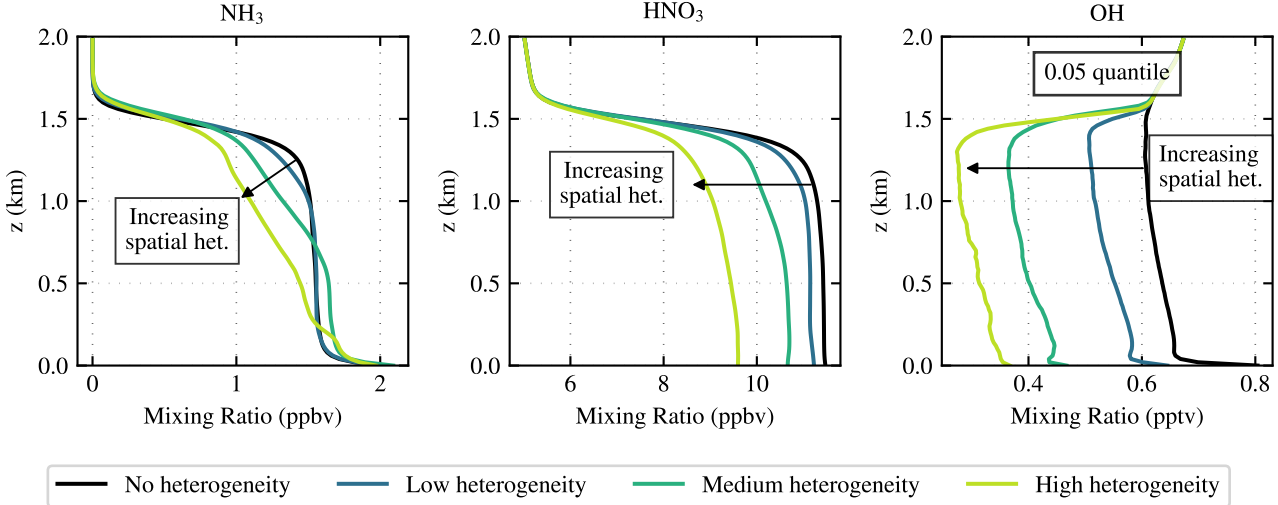


Figure 3. Vertical profiles of gas phase species NH_3 (left), HNO_3 (center), and OH (right) at $t = 6$ h. For NH_3 (left) and HNO_3 , the mean value is displayed at each vertical level. For OH , the 5th percentile at each vertical level is shown to indicate the local changes to the OH mixing ratio near the emissions plume. Values for the no heterogeneity scenario are shown as a solid black line while emissions scenarios 1–3 are shown as colored solid lines.

acid mixing ratios decrease on average. As will be demonstrated in Section 3.3, this is due to increased partitioning of these species into the aerosol phase to form ammonium nitrate.

For OH , the vertical profiles show the 5th percentile of mixing ratio within each level, rather than the domain-wise mean, to better capture localized depletion near the emissions plume. Scenarios with high emissions spatial heterogeneity result in a pronounced reduction in OH near the emissions plume. Whereas in the no heterogeneity scenario, the level-mean mixing ratio of OH is 0.61 pptv at $z = 1$ km, whereas in the high heterogeneity scenario they drop by 54% to 0.28 pptv.

3.2 Aerosol size distributions

Number and mass distributions for each emissions scenario are shown in Figure 4. Each size distribution is taken from a vertical level in the upper boundary layer at $z \approx 800$ m. When analyzing size distributions for a single grid cell, considerable stochastic noise is present in the shape of distributions. This is due to the selected number of computational particles per grid cell ($N = 100$) alongside the stochastic treatment of aerosol particles in WRF-PartMC. To reduce stochastic noise, number and mass distributions represent the average distribution in a 1 km^2 region centered over the emissions plume (i.e., size distributions are averaged over a 10×10 grid cell region). For the no heterogeneity scenario, the medium heterogeneity scenario, and the high heterogeneity scenario, this region is directly over the center of the domain. For the low heterogeneity scenario, emissions are released in one half of the domain that is offset from the center, and thus the averaging region is located in the center of the

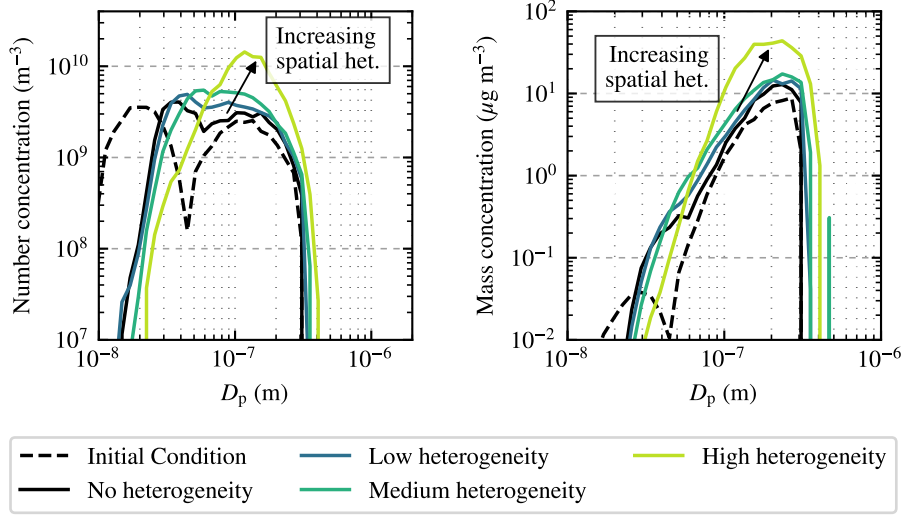


Figure 4. Number (left) and mass (right) distributions for each emissions scenario in the upper boundary layer ($z = 800$) m and $t = 6$ h. The initial condition is shown as the dashed black line. Values for the no heterogeneity scenario are shown as a solid black line while emissions scenarios 1–3 are shown as colored solid lines.

215 emissions patch. For each size distribution, data have been binned into 100 logarithmically spaced bins, ranging in size from 10^{-9} to 10^{-3} m.

To quantify changes in particle populations, the number and mass concentration of Aitken ($D_p \leq 50$ nm) and accumulation ($D_p > 50$ nm) mode particles were calculated. As the spatial heterogeneity of emissions increases, the number of Aitken mode particles decreases by up to 81% while the number of accumulation mode particles increases by up to 246%. The decrease in 220 Aitken mode particles is attributable to enhanced Brownian coagulation due to higher local concentrations near the emissions plume core. The corresponding increase in accumulation mode particles is a result of secondary aerosol formation. Changes to aerosol composition due to gas-particle partitioning is explored in further detail in the next section.

Similarly, the mass distribution of Aitken mode particles decreases by up to 74% for high emissions spatial heterogeneity scenarios, while the accumulation mode mass fraction increases by up to 309%. Coagulation of smaller Aitken mode particles 225 with accumulation mode particles contributes little change in the mass distribution as indicated by a slight reduction in the Aitken mode mass concentration. Alongside the increase in the number of accumulation mode particles, the increase in mass concentration among these particles is due to gas-particle partitioning.

3.3 Aerosol composition

Figure 5 shows cross sections of aerosol ammonium, nitrate, and sulfate in the upper boundary layer ($z \approx 900$ m) at $t = 6$ h. The 230 spatial distribution of ammonium and nitrate closely follow the emissions plume, indicating that ammonium nitrate formation occurs where ammonia and nitric acid are abundant. In these regions, excess gas phase concentrations drive partitioning into the

aerosol phase. Further out from the emissions plume, ammonium and nitrate concentrations quickly fall off as the equilibrium condition shifts to the gas phase.

In contrast, sulfate is more uniformly distributed across all scenarios, resulting in lower spatial heterogeneity for the high heterogeneity scenario ($\eta = 0.021$) compared to ammonium ($\eta = 0.142$) and nitrate ($\eta = 0.739$). This is due to the extremely low volatility of sulfuric acid which remains almost entirely in the aerosol phase as sulfate regardless of proximity to the emissions plume. Unlike ammonia and nitric acid, which partition dynamically between the gas and aerosol phase, sulfate does not re-enter the gas phase. Consequently, the spatial distribution of aerosol species is determined by their volatility, with less volatile species exhibiting more uniform distributions, while higher volatility species remain clustered near plumes with high concentrations of corresponding gas phase precursors. Given the sensitivity of nitrate formation to the spatial heterogeneity of emissions, nitrate levels are extremely low in the no heterogeneity scenario, with most grid cells containing no nitrate. Occasionally, some grid cells may briefly contain particles with nitrate. For the spatial heterogeneity metric, this is akin to the point source scenario. As a result, the spatial heterogeneity of nitrate for the no heterogeneity scenario appears higher ($\eta = 0.513$) than the value of η for ammonium and sulfate ($\eta = 0.010$ and $\eta = 0.011$, respectively).

Figure 6 shows vertical profiles of aerosol ammonium (NH_4^+), nitrate (NO_3^-), and sulfate (SO_4^{2-}) for each emissions scenario. These profiles represent the average concentrations within each vertical level at the end of each simulation ($t = 6$ h).

Sulfate concentrations are nearly uniform within the boundary layer and rapidly decrease above the entrainment zone due to limited mixing between the free troposphere and boundary layer. Sulfate concentrations decrease as the emissions spatial heterogeneity increases. Production of sulfate relies on the oxidation of SO_2 by OH. Within the high concentration environment of the emissions plume, many reactive gas phase compounds including volatile organic compounds (VOCs) compete alongside SO_2 for oxidation. With OH rapidly depleted near the emissions plume, oxidation of SO_2 into H_2SO_4 proceeds at a slower rate, reducing sulfate formation. OH from outside the emissions plume is not mixed fast enough into the plume to restore its concentration (see Figure 2). Thus, segregation of OH and SO_2 alters sulfate production due to the spatial heterogeneity of emissions.

Both ammonium and nitrate concentrations increase with height in the boundary layer due to the strong temperature dependence of ammonium nitrate formation. Nitrate availability depends on the presence of free ammonia, i.e., ammonia not already neutralizing sulfate as ammonium sulfate. In the lowest 500 m of the boundary layer, the concentration of NH_4^+ decreases under high emissions spatial heterogeneity due to lower sulfate concentrations at higher emissions spatial heterogeneity.

At higher altitudes ($z \sim 1.2$ km), ammonium nitrate formation is enhanced for scenarios with high emissions spatial heterogeneity. Under these conditions, the concentration of free ammonia increases due to lower sulfate levels, allowing neutralization of more nitric acid. In the no heterogeneity scenario, little nitrate is formed due to the overall lower concentrations of nitric acid and ammonia, pushing their equilibrium partitioning to the gas phase. This indicates the strong dependence of nitrate concentrations on the composition of the aerosol and the level of emissions spatial heterogeneity.

Figure 7 shows the size-resolved mass fraction of aerosols in the upper boundary layer ($z \approx 800$ m) for the initial condition and at the end of simulations ($t = 6$ h) for both the no heterogeneity scenario and the high heterogeneity scenario. After 6 hours, significant differences in composition emerge. Under uniform emissions, particles mainly consist of BC and primary

organic aerosol (POA) along with some sulfate. By contrast, particles in the high heterogeneity scenario are dominated by nitrate, ammonium, and sulfate, which together comprise 50–80% of aerosol mass.

The CCN activity of particles in the size range of 50–100 nm is largely governed by their composition. Figure 7 indicates that, for the no heterogeneity scenario, particles in this size range are primarily composed of low hygroscopicity compounds, including BC and POA. In the high heterogeneity scenario, the dominant presence of sulfate, nitrate, and ammonium increases particle hygroscopicity. This suggests that particles in the size range of 50–100 nm, whose CCN activity depends on aerosol composition, exhibit greater hygroscopicity under high emissions spatial heterogeneity, allowing them to activate at lower supersaturations. We show this is indeed the case by evaluating changes in the 2-dimensional number distribution $n(D_p, \kappa)$ as a function of particle diameter D_p and particle hygroscopicity parameter κ .

Figure 8 shows 2-dimensional number distributions $n(D_p, \kappa)$ for emissions scenario extremes. Each distribution was sampled in the upper boundary layer ($z \approx 800$ m) at the beginning and end of simulations. Initially, all particles possess the same composition and thus the same hygroscopicity. The right panel compares distributions at $t = 6$ h for the no heterogeneity scenario and the high heterogeneity scenario.

In the no heterogeneity scenario, two distinct particle groups emerge: one with low κ values (0–0.3), corresponding to primary carbonaceous aerosols that have not undergone significant aging, and another with higher κ (0.3–0.6), representing particles that have undergone coagulation and gas-particle partitioning. The latter group is enriched in sulfate as seen in Figure 7.

In the high heterogeneity scenario, particles exhibit significantly higher hygroscopicities. For instance, the hygroscopicity of particles with diameter of 100 nm exceeds $\kappa > 0.6$ (indicating highly hygroscopic particles), whereas κ only reaches up to 0.4 in the no heterogeneity scenario. As suggested in discussing the link between aerosol composition and CCN activity for particles in the size range of $D_p \sim 50\text{--}100$ nm, this indicates that spatially heterogeneous emissions indeed lower the critical supersaturation of such particles, enhancing their CCN activity.

Differences in the κ distributions between the no heterogeneity scenario and the high heterogeneity scenario stem from the interaction between emissions spatial heterogeneity and sub-grid scale aerosol processes. Enhanced coagulation in emissions plumes reduces Aitken mode particle concentrations, explaining the absence of a low- κ carbonaceous aerosol group in the high heterogeneity scenario. Furthermore, spatially heterogeneous emissions promote gas-particle partitioning, increasing particle hygroscopicity. In particular, higher concentrations of nitric acid and ammonia near spatially heterogeneous emissions plumes drive the equilibrium condition into the aerosol phase, raising the concentration of ammonium nitrate alongside particle hygroscopicity.

3.4 CCN activity

Figure 9 shows vertical profiles of the CCN number per kilogram of dry air for environmental supersaturations S_{env} ranging from $S_{\text{env}} = 0.1\%$ to $S_{\text{env}} = 1.0\%$ across different emissions scenario. Since the ambient relative humidity (RH) never exceeds 100% in these simulations, the reported CCN concentrations represent the number of particles that would activate if RH were raised to the specified supersaturation.

As noted earlier, emissions spatial heterogeneity influences aerosol processes such as coagulation and gas-particle partitioning, altering the particle number, size, composition, and hygroscopicity. In turn, these modifications impact CCN activity, though the dominant processes and their effects vary with supersaturation.

At lower supersaturations ($S_{\text{env}} = 0.1\text{--}0.3\%$), CCN concentrations increases with emissions spatial heterogeneity in the upper boundary layer. This is due to enhanced formation of ammonium nitrate in the cooler, sulfate-poor environment, which increases activation of ultrafine particles in the range of 50–100 nm due to the high hygroscopicity of ammonium nitrate.

At higher supersaturations ($S_{\text{env}} = 0.6\text{--}1.0\%$), CCN concentrations still increase in the upper boundary layer for scenarios with lower spatial heterogeneity, however, in the high heterogeneity scenario, CCN concentrations decrease, particularly at $S_{\text{env}} = 1.0\%$, where CCN concentrations drop below all other scenarios including the no heterogeneity scenario. This is due to enhanced coagulation in highly heterogeneous emissions scenarios which reduces the number of smaller particles that would otherwise activate at high supersaturations. Therefore, at sufficiently high supersaturation and emissions spatial heterogeneity, the negative effect on CCN concentration due to coagulation offsets the positive effect of gas-particle partitioning of hygroscopic material.

Figure 10 illustrates the temporal and vertical evolution of the percent difference between the CCN concentrations relative to the no heterogeneity scenario for each scenario and supersaturation level. The percent difference is calculated as

$$\% \text{ difference} \left([\overline{\text{CCN}}]_{\text{Scenario}}, [\overline{\text{CCN}}]_{\text{No heterogeneity}} \right) = 100 \times \left(\frac{[\overline{\text{CCN}}](t, z, S_{\text{env}})_{\text{Scenario}} - [\overline{\text{CCN}}](t, z, S_{\text{env}})_{\text{No heterogeneity}}}{[\overline{\text{CCN}}](t, z, S_{\text{env}})_{\text{No heterogeneity}}} \right), \quad (2)$$

where $[\overline{\text{CCN}}](t, z, S_{\text{env}})$ is the horizontally averaged concentration of CCN at time t and vertical level z that activate at supersaturation S_{env} .

The greatest increase in CCN concentration relative to the no heterogeneity scenario occurs in the high heterogeneity scenario at $S_{\text{env}} = 0.3\%$, where CCN concentrations increase by more than 25% through $t = 6$ h. At both high supersaturations and high emissions spatial heterogeneity, the reduction in CCN activity due to enhanced coagulation becomes evident after $t \approx 5$ h. Across all scenarios, CCN concentrations increase most near the top of the boundary layer. This region grows with time due to boundary layer development. Notably, shallow cumuli and stratiform clouds tend to form in the upper boundary layer. This suggests that emissions spatial heterogeneity could enhance cloud albedo through the first indirect effect.

325 3.5 Influence of ammonia on aerosol composition and CCN activity

To further explore the role of ammonia in CCN activity under spatially heterogeneous emissions, we conducted additional simulations for the no heterogeneity scenario and the high heterogeneity scenario, setting total ammonium ($\text{NH}_3, \text{gas} + \text{NH}_4, \text{aerosol}$) to zero. Correspondingly, emissions of NH_3 were set to zero to ensure that total ammonium remains zero throughout each simulation.

330 Figure 11 shows vertical profiles of CCN mixing ratios at $t = 6$ h for supersaturations ranging from $S_{\text{env}} = 0.1\%$ to $S_{\text{env}} = 1.0\%$. Without ammonia, CCN concentrations at each supersaturation level agree much more closely between the no heterogeneity scenario and the high heterogeneity scenario. The peak of CCN concentrations in the upper boundary layer and at lower supersaturations, previously observed in the high heterogeneity scenario, disappears entirely. This underscores

the crucial role of ammonium nitrate formation in modulating CCN concentrations under spatially heterogeneous emissions,

335 especially at lower supersaturations.

At higher supersaturations ($S_{\text{env}} = 1.0\%$), the high heterogeneity scenario exhibits lower CCN concentrations than the ammonia-free no heterogeneity scenario. This further confirms that, in the absence of ammonia-driven gas-particle partitioning, coagulation-induced particle loss dominates, leading to an overall reduction in the concentration of CCN. The similarity in CCN profiles between the ammonia-free cases of the high heterogeneity scenario and the no heterogeneity scenario, apart from
340 a slight (5%) downward shift in the high heterogeneity scenario due to enhanced coagulation, underscores the competing influences of emissions spatial heterogeneity on aerosol-cloud interactions.

4 Limitations

This study is based on highly idealized simulations, which were designed to isolate the role of emissions spatial heterogeneity under controlled meteorological conditions. While this allows for a clear attribution of observed effects to aerosol processes
345 such as coagulation and gas-particle partitioning, it also introduces limitations. First, the simulations assume a horizontally homogeneous land surface, no synoptic-scale forcing, and a fixed solar heating profile, which neglects the potential influence of surface heterogeneity, wind shear, and diurnal variability. Second, all emissions—both gas-phase and particulate—are temporally constant after spin-up and spatially collocated, which may not reflect the complexity of real urban emission patterns where different sources (e.g., traffic, industry, biomass burning) are spatially and temporally decoupled. Third, while the chosen
350 aerosol composition is grounded in past urban measurements (SCAQS), the limited diversity in primary aerosol types and the exclusion of additional chemical pathways (e.g., aqueous-phase oxidation) constrain the generalizability of the results. Finally, the computational particle count per grid cell ($N_p = 100$) and the fixed domain size may underrepresent stochastic variability in some fine-scale processes, particularly at early times or near the plume edge. These limitations motivate future work incorporating more realistic emissions, meteorological variability, and extended simulation times to evaluate the robustness of the
355 conclusions presented here.

5 Conclusions

This study investigates the impact of spatially heterogeneous emissions on aerosol properties, including CCN activity, in a convective boundary layer using the particle-resolved large-eddy simulation modeling framework, WRF-PartMC-MOSAIC-LES. This first-of-its-kind modeling platform enables a detailed process-level analysis of the coupling between emissions spatial
360 heterogeneity and concentration-dependent aerosol processes such as coagulation and gas-particle partitioning. To assess these interactions, we compare multiple idealized emissions scenarios against a base case of uniform emissions, which serves as a proxy for coarser-resolved models that lack the ability to resolve heterogeneity of emissions.

Our results demonstrate that emissions spatial heterogeneity significantly alters key aerosol processes. In particular, nitrate formation increases substantially in regions of high emissions heterogeneity due to localized enhancements in nitric acid and

365 ammonia concentrations near the emissions plume core. This shifts the equilibrium favoring ammonium nitrate formation in the aerosol phase. In turn, the volatility of aerosol species is coupled with the spatial heterogeneity of emissions and precursor species. Low-volatility compounds such as sulfate are more spatially homogeneous due to their tendency to remain in the aerosol phase even as particles are transported away from the emissions plume. Additionally, higher emissions heterogeneity intensifies coagulation, accelerating particle growth and modifying the size distribution of aerosols.

370 These aerosol process changes have downstream effects on CCN activity. Notably, the influence of emissions spatial heterogeneity on CCN concentrations is governed by competing effects of coagulation and gas-particle partitioning. Coagulation removes smaller particles that would otherwise activate at high supersaturations, resulting in a decrease in CCN activity at high supersaturations for scenarios with high emissions spatial heterogeneity. Conversely, coagulation is not as efficient at removing larger particles that activate at lower supersaturations. In contrast, gas-particle partitioning results in an increase of highly
375 hygroscopic compounds such as ammonium nitrate under high emissions spatial heterogeneity. As a result, CCN activity at lower supersaturations ($S_{\text{env}} = 0.3\text{--}0.6\%$) increases by up to 25% in the upper boundary layer for emissions scenarios with high spatial heterogeneity.

The sensitivity of CCN activity to emissions spatial heterogeneity is highly influenced by the aerosol and gas phase composition. Given the key contribution of ammonium nitrate formation in elevating CCN activity under highly spatially heterogeneous scenarios, removing ammonia weakens—or in some cases reverses—the trend between emissions spatial heterogeneity and CCN concentrations.
380

This has important implications for global climate models, where nitrate formation is often simplified by assuming equilibrium partitioning or omitted altogether. Our findings highlight the necessity of accurately representing nitrate in global climate models due to the strong coupling between emissions spatial heterogeneity, aerosol composition, and CCN activity. As model
385 resolution continues to improve, advancing the representation of aerosol chemistry will be critical to capturing the full impact of emissions spatial heterogeneity on cloud microphysics and climate.

This study uses highly idealized emission patterns, in which all sources are spatially collocated, and a limited set of aerosol types under fixed meteorological conditions. While our results show that aerosol composition mediates the impact of spatial heterogeneity on properties such as CCN activity, future work should expand this analysis to more realistic scenarios. In
390 particular, it will be important to examine cases with spatially separated emission sources, a broader diversity of primary aerosol types, and a range of meteorological conditions that influence transport, mixing, and cloud formation. Such studies will help determine the generality of our findings across different geographic settings, including urban, agricultural, and remote regions.

Code and data availability. WRF-PartMC is open source and maintained on GitHub: <https://github.com/open-atmos/wrf-partmc.git>. The
395 version of WRF-PartMC used in this paper was coupled with the multiphase chemistry model MOSAIC and custom initialization code was written for specifying the emissions initial conditions unique to each emissions scenario alongside specific namelist configurations for particle-resolved LES. The model code (including the WRF base model v3.9.1, PartMC aerosol model v2.6.1, and MOSAIC chem-

istry model) used for this publication has been archived on Zenodo with the following DOI: <https://doi.org/10.5281/zenodo.16850289>. All simulation outputs and scripts used to generate figures in this paper are available via the Illinois Data Bank: https://doi.org/10.13012/B2IDB-9622921_V1.

400

Author contributions. SGF designed the modeling scenarios, developed code for implementing WRF-PartMC-MOSAIC-LES, performed analysis of model outputs and produced manuscript figures, and led the drafting of the manuscript. JHC provided consultation and guidance for the development of initialization code in extending WRF-PartMC to LES scenarios. MM led the conceptualization and implementation of the spatial heterogeneity metric. MW provided overall guidance and project conceptualization. NR provided guidance, contributed to con-

405ceptualization, and collaborated with SF in the drafting of the introduction (Section 1), limitations (Section 4), and conclusions (Section 5).

All authors contributed to editing.

Competing interests. The authors declare that they have no conflict of interest.

Acknowledgements. This material is based upon work supported by the U.S. Department of Energy, Office of Science, Office of Biological and Environmental Research under Award Number DE-SC0022130, and by the National Science Foundation Grant Number AGS 19-41110.

410 **References**

- Brasseur, G. P., Barth, M., Kazil, J., Patton, E., and Wang, Y.: Segregation of Fast-Reactive Species in Atmospheric Turbulent Flow, <https://doi.org/10.20944/preprints202305.0895.v1>, 2023.
- Ching, J., Fast, J., West, M., and Riemer, N.: Metrics to quantify the importance of mixing state for CCN activity, *Atmospheric Chemistry and Physics*, 17, 7445–7458, <https://doi.org/10.5194/acp-17-7445-2017>, publisher: Copernicus GmbH, 2017.
- 415 Crippa, P., Sullivan, R. C., Thota, A., and Pryor, S. C.: The impact of resolution on meteorological, chemical and aerosol properties in regional simulations with WRF-Chem, *Atmospheric Chemistry and Physics*, 17, 1511–1528, <https://doi.org/10.5194/acp-17-1511-2017>, publisher: Copernicus GmbH, 2017.
- Curtis, J. H., Riemer, N., and West, M.: A single-column particle-resolved model for simulating the vertical distribution of aerosol mixing state: WRF-PartMC-MOSAIC-SCM v1.0, *Geoscientific Model Development*, 10, 4057–4079, <https://doi.org/10.5194/gmd-10-4057-2017>, publisher: Copernicus GmbH, 2017.
- 420 Curtis, J. H., Riemer, N., and West, M.: Explicit stochastic advection algorithms for the regional-scale particle-resolved atmospheric aerosol model WRF-PartMC (v1.0), *Geoscientific Model Development*, 17, 8399–8420, <https://doi.org/10.5194/gmd-17-8399-2024>, 2024.
- de Bruine, M., Krol, M., Vilà-Guerau de Arellano, J., and Röckmann, T.: Explicit aerosol–cloud interactions in the Dutch Atmospheric Large-Eddy Simulation model DALES4.1-M7, *Geoscientific Model Development*, 12, 5177–5196, <https://doi.org/10.5194/gmd-12-5177-2019>, publisher: Copernicus GmbH, 2019.
- 425 Deardorff, J. W.: Stratocumulus-capped mixed layers derived from a three-dimensional model, *Boundary-Layer Meteorology*, 18, 495–527, <https://doi.org/10.1007/BF00119502>, 1980.
- Fierce, L., Riemer, N., and Bond, T. C.: When is cloud condensation nuclei activity sensitive to particle characteristics at emission?, *Journal of Geophysical Research: Atmospheres*, 118, 13,476–13,488, <https://doi.org/10.1002/2013JD020608>, _eprint: <https://onlinelibrary.wiley.com/doi/pdf/10.1002/2013JD020608>, 2013.
- 430 Fierce, L., Riemer, N., and Bond, T. C.: Explaining variance in black carbon's aging timescale, *Atmospheric Chemistry and Physics*, 15, 3173–3191, <https://doi.org/10.5194/acp-15-3173-2015>, publisher: Copernicus GmbH, 2015.
- Fierce, L., Yao, Y., Easter, R., Ma, P.-L., Sun, J., Wan, H., and Zhang, K.: Quantifying structural errors in cloud condensation nuclei activity from reduced representation of aerosol size distributions, *Journal of Aerosol Science*, 181, 106388, <https://doi.org/10.1016/j.jaerosci.2024.106388>, 2024.
- 435 Forster, P., Storelvmo, T., Armour, K., Collins, W., Dufresne, J.-L., Frame, D., Lunt, D., Mauritsen, T., Palmer, M., Watanabe, M., Wild, M., and Zhang, H.: The Earth's Energy Budget, Climate Feedbacks, and Climate Sensitivity, p. 923–1054, Cambridge University Press, Cambridge, United Kingdom and New York, NY, USA, <https://doi.org/10.1017/9781009157896.009>, 2021.
- Golaz, J., Van Roekel, L. P., Zheng, X., Roberts, A. F., Wolfe, J. D., Lin, W., Bradley, A. M., Tang, Q., Maltrud, M. E., Forsyth, R. M., Zhang, C., Zhou, T., Zhang, K., Zender, C. S., Wu, M., Wang, H., Turner, A. K., Singh, B., Richter, J. H., Qin, Y., Petersen, M. R., Mametjanov, A., Ma, P., Larson, V. E., Krishna, J., Keen, N. D., Jeffery, N., Hunke, E. C., Hannah, W. M., Guba, O., Griffin, B. M., Feng, Y., Engwirda, D., Di Vittorio, A. V., Dang, C., Conlon, L. M., Chen, C., Brunke, M. A., Bisht, G., Benedict, J. J., Asay-Davis, X. S., Zhang, Y., Zhang, M., Zeng, X., Xie, S., Wolfram, P. J., Vo, T., Veneziani, M., Tesfa, T. K., Sreepathi, S., Salinger, A. G., Reeves Eyre, J. E. J., Prather, M. J., Mahajan, S., Li, Q., Jones, P. W., Jacob, R. L., Huebler, G. W., Huang, X., Hillman, B. R., Harrop, B. E., Foucar, J. G., Fang, Y., Comeau, D. S., Caldwell, P. M., Bartoletti, T., Balaguru, K., Taylor, M. A., McCoy, R. B., Leung, L. R., and Bader, D. C.: The DOE
- 440
- 445

E3SM Model Version 2: Overview of the Physical Model and Initial Model Evaluation, *Journal of Advances in Modeling Earth Systems*, 14, e2022MS003 156, <https://doi.org/10.1029/2022MS003156>, 2022.

Gustafson Jr., W. I., Qian, Y., and Fast, J. D.: Downscaling aerosols and the impact of neglected subgrid processes on direct aerosol radiative forcing for a representative global climate model grid spacing, *Journal of Geophysical Research: Atmospheres*, 116, 450 <https://doi.org/10.1029/2010JD015480>, 2011.

Kaser, L., Karl, T., Yuan, B., Mauldin III, R. L., Cantrell, C. A., Guenther, A. B., Patton, E. G., Weinheimer, A. J., Knotz, C., Orlando, J., Emmons, L., Apel, E., Hornbrook, R., Shertz, S., Ullmann, K., Hall, S., Graus, M., de Gouw, J., Zhou, X., and Ye, C.: Chemistry-turbulence interactions and mesoscale variability influence the cleansing efficiency of the atmosphere, *Geophysical Research Letters*, 42, 10,894–10,903, <https://doi.org/10.1002/2015GL066641>, _eprint: <https://onlinelibrary.wiley.com/doi/pdf/10.1002/2015GL066641>, 2015.

455 Kokkola, H., Korhonen, H., Lehtinen, K. E. J., Makkonen, R., Asmi, A., Järvenoja, S., Anttila, T., Partanen, A.-I., Kulmala, M., Järvinen, H., Laaksonen, A., and Kerminen, V.-M.: SALSA – a Sectional Aerosol module for Large Scale Applications, *Atmospheric Chemistry and Physics*, 8, 2469–2483, <https://doi.org/10.5194/acp-8-2469-2008>, publisher: Copernicus GmbH, 2008.

Kurppa, M., Hellsten, A., Roldin, P., Kokkola, H., Tonttila, J., Auvinen, M., Kent, C., Kumar, P., Maronga, B., and Järvi, L.: Implementation of the sectional aerosol module SALSA2.0 into the PALM model system 6.0: model development and first evaluation, *Geoscientific Model Development*, 12, 1403–1422, <https://doi.org/10.5194/gmd-12-1403-2019>, publisher: Copernicus GmbH, 2019.

460 Lin, G., Qian, Y., Yan, H., Zhao, C., Ghan, S. J., Easter, R., and Zhang, K.: Quantification of marine aerosol subgrid variability and its correlation with clouds based on high-resolution regional modeling, *Journal of Geophysical Research: Atmospheres*, 122, 6329–6346, <https://doi.org/10.1002/2017JD026567>, 2017.

Liu, Y., Yao, Y., Curtis, J. H., West, M., and Riemer, N.: The impacts of aerosol mixing state on heterogeneous N₂O₅ hydrolysis, *Aerosol Science and Technology*, 59, 402–423, <https://doi.org/10.1080/02786826.2024.2443587>, 2025.

Ma, P.-L., Rasch, P. J., Wang, M., Wang, H., Ghan, S. J., Easter, R. C., Gustafson Jr., W. I., Liu, X., Zhang, Y., and Ma, H.-Y.: How does increasing horizontal resolution in a global climate model improve the simulation of aerosol-cloud interactions?, *Geophysical Research Letters*, 42, 5058–5065, <https://doi.org/10.1002/2015GL064183>, _eprint: <https://onlinelibrary.wiley.com/doi/pdf/10.1002/2015GL064183>, 2015.

470 Mohebalhojeh, M., Frederick, S., Riemer, N., and West, M.: A Measure of Spatial Heterogeneity, (Manuscript in preparation), 2025.

Ouwersloot, H. G., Vilà-Guerau de Arellano, J., van Heerwaarden, C. C., Ganzeveld, L. N., Krol, M. C., and Lelieveld, J.: On the segregation of chemical species in a clear boundary layer over heterogeneous land surfaces, *Atmospheric Chemistry and Physics*, 11, 10 681–10 704, <https://doi.org/10.5194/acp-11-10681-2011>, publisher: Copernicus GmbH, 2011.

475 Qian, Y., Gustafson, W. I. J., and Fast, J. D.: An investigation of the sub-grid variability of trace gases and aerosols for global climate modeling, *Atmospheric Chemistry and Physics*, 10, 6917–6946, <https://doi.org/10.5194/acp-10-6917-2010>, publisher: Copernicus GmbH, 2010.

Riemer, N., West, M., Zaveri, R. A., and Easter, R. C.: Simulating the evolution of soot mixing state with a particle-resolved aerosol model, *Journal of Geophysical Research: Atmospheres*, 114, <https://doi.org/10.1029/2008JD011073>, 2009.

480 Skamarock, C., Klemp, B., Dudhia, J., Gill, O., Barker, D., Duda, G., Huang, X.-y., Wang, W., and Powers, G.: A Description of the Advanced Research WRF Version 3, <https://doi.org/10.5065/D68S4MVH>, 2008.

Stull, R. B.: An Introduction to Boundary Layer Meteorology, Atmospheric sciences library, Kluwer Academic Publishers, Dordrecht, ISBN 978-90-277-2768-8, Section 7.1, Page 252, 1988.

Tilmes, S., Mills, M. J., Zhu, Y., Bardeen, C. G., Vitt, F., Yu, P., Fillmore, D., Liu, X., Toon, B., and Deshler, T.: Description and performance of a sectional aerosol microphysical model in the Community Earth System Model (CESM2), *Geoscientific Model Development*, 16, 6087–6125, <https://doi.org/10.5194/gmd-16-6087-2023>, publisher: Copernicus GmbH, 2023.

485 Tonttila, J., Maalick, Z., Raatikainen, T., Kokkola, H., Kühn, T., and Romakkaniemi, S.: UCLALES-SALSA v1.0: a large-eddy model with interactive sectional microphysics for aerosol, clouds and precipitation, *Geoscientific Model Development*, 10, 169–188, <https://doi.org/10.5194/gmd-10-169-2017>, publisher: Copernicus GmbH, 2017.

Vignati, E., Wilson, J., and Stier, P.: M7: An efficient size-resolved aerosol microphysics module for large-scale aerosol transport models, *Journal of Geophysical Research: Atmospheres*, 109, <https://doi.org/10.1029/2003JD004485>, _eprint: <https://onlinelibrary.wiley.com/doi/pdf/10.1029/2003JD004485>, 2004.

Weigum, N., Schutgens, N., and Stier, P.: Effect of aerosol subgrid variability on aerosol optical depth and cloud condensation nuclei: implications for global aerosol modelling, *Atmospheric Chemistry and Physics*, 16, 13 619–13 639, <https://doi.org/10.5194/acp-16-13619-2016>, publisher: Copernicus GmbH, 2016.

495 Zaveri, R. A. and Peters, L. K.: A new lumped structure photochemical mechanism for large-scale applications, *Journal of Geophysical Research: Atmospheres*, 104, 30 387–30 415, <https://doi.org/10.1029/1999JD900876>, 1999.

Zaveri, R. A., Easter, R. C., and Peters, L. K.: A computationally efficient Multicomponent Equilibrium Solver for Aerosols (MESA), *Journal of Geophysical Research: Atmospheres*, 110, <https://doi.org/10.1029/2004JD005618>, 2005a.

500 Zaveri, R. A., Easter, R. C., and Wexler, A. S.: A new method for multicomponent activity coefficients of electrolytes in aqueous atmospheric aerosols, *Journal of Geophysical Research: Atmospheres*, 110, <https://doi.org/10.1029/2004JD004681>, _eprint: <https://onlinelibrary.wiley.com/doi/pdf/10.1029/2004JD004681>, 2005b.

Zaveri, R. A., Easter, R. C., Fast, J. D., and Peters, L. K.: Model for Simulating Aerosol Interactions and Chemistry (MOSAIC), *Journal of Geophysical Research: Atmospheres*, 113, <https://doi.org/10.1029/2007JD008782>, 2008.

505 Zaveri, R. A., Barnard, J. C., Easter, R. C., Riemer, N., and West, M.: Particle-resolved simulation of aerosol size, composition, mixing state, and the associated optical and cloud condensation nuclei activation properties in an evolving urban plume, *Journal of Geophysical Research: Atmospheres*, 115, <https://doi.org/10.1029/2009JD013616>, 2010.

510 Zaveri, R. A., Easter, R. C., Singh, B., Wang, H., Lu, Z., Tilmes, S., Emmons, L. K., Vitt, F., Zhang, R., Liu, X., Ghan, S. J., and Rasch, P. J.: Development and Evaluation of Chemistry-Aerosol-Climate Model CAM5-Chem-MAM7-MOSAIC: Global Atmospheric Distribution and Radiative Effects of Nitrate Aerosol, *Journal of Advances in Modeling Earth Systems*, 13, e2020MS002346, <https://doi.org/10.1029/2020MS002346>, _eprint: <https://onlinelibrary.wiley.com/doi/pdf/10.1029/2020MS002346>, 2021.

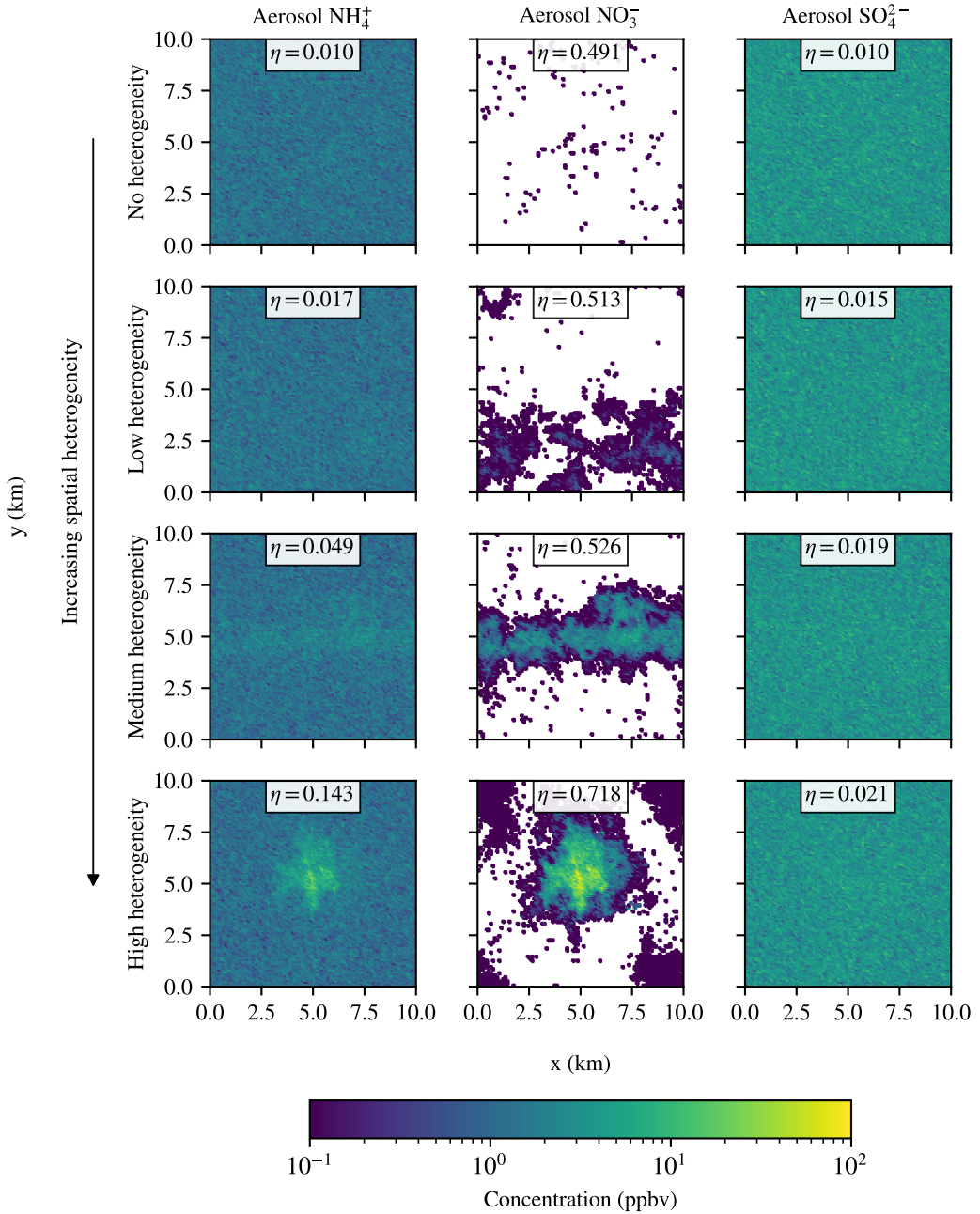


Figure 5. Cross sections in the x-y plane of aerosol species NH_4^+ (left column), NO_3^- (center column), and SO_4^{2-} (right column). Cross sections are shown at a height of approximately $z \approx 900$ m and at $t = 6$ h. Coloring indicates the mixing ratio of aerosol species in parts per billion by volume. Regions below a trace mixing ratio of 10 pptv are filled in white. The value of the spatial heterogeneity metric η is displayed alongside each cross section plot.

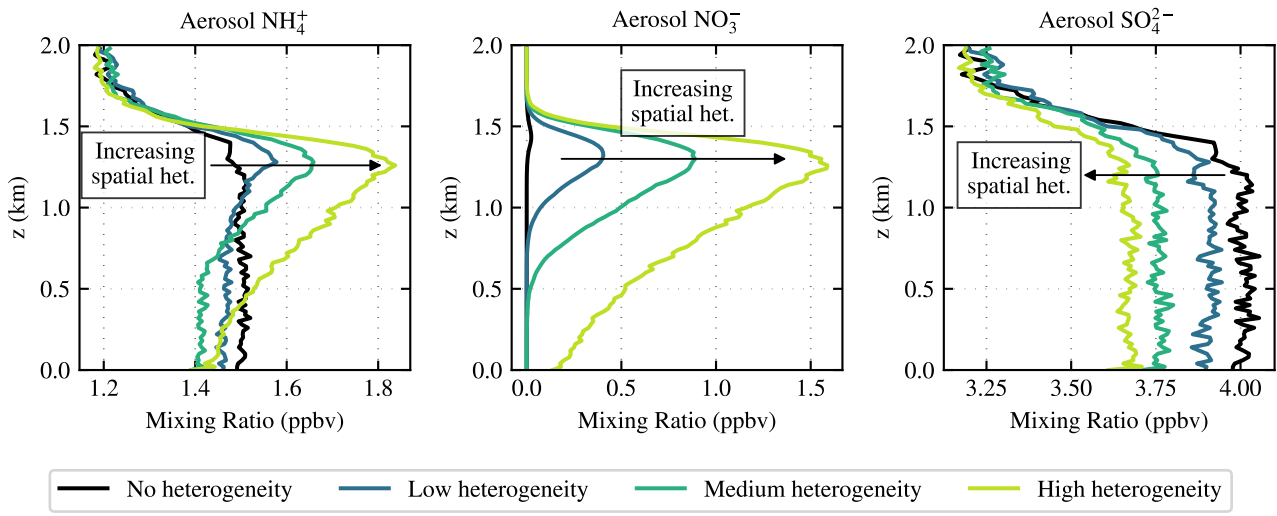


Figure 6. Vertical profiles of aerosol species NH_4^+ (left), NO_3^- (center), and SO_4^{2-} (right) at $t = 6$ h and in parts per billion by volume (ppbv). For each compound, the mean value is displayed at each vertical level. Values for the no heterogeneity scenario are shown as a solid black line while emissions scenarios 1–3 are shown as colored solid lines.

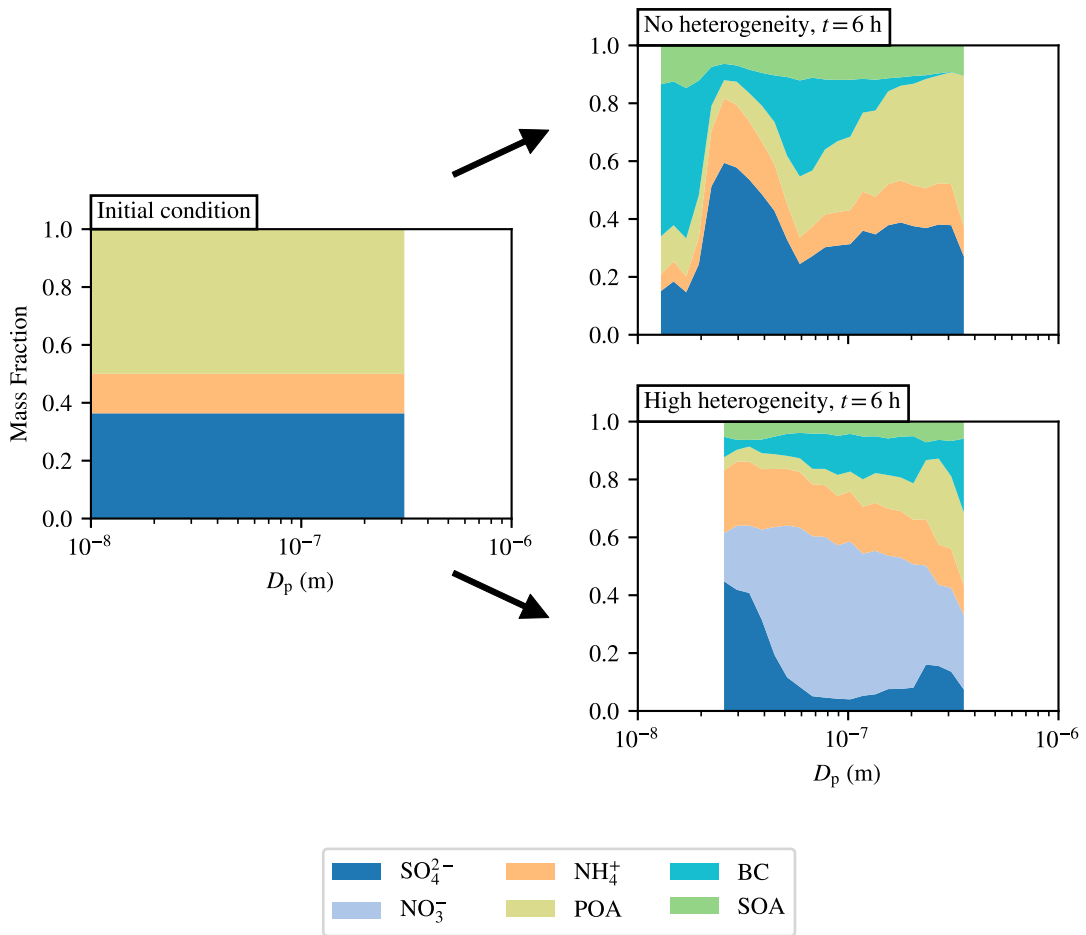


Figure 7. Speciated mass fraction as a function of particle diameter for emissions scenario extremes (no heterogeneity scenario and high heterogeneity scenario). The initial condition is shown on the left, indicating that aerosol begin as an equal mixture of POA and ammonium sulfate. On the right, emissions scenarios with minimum spatial heterogeneity (top, no heterogeneity scenario) and maximum spatial heterogeneity (bottom, high heterogeneity scenario) are shown after 6 hours.

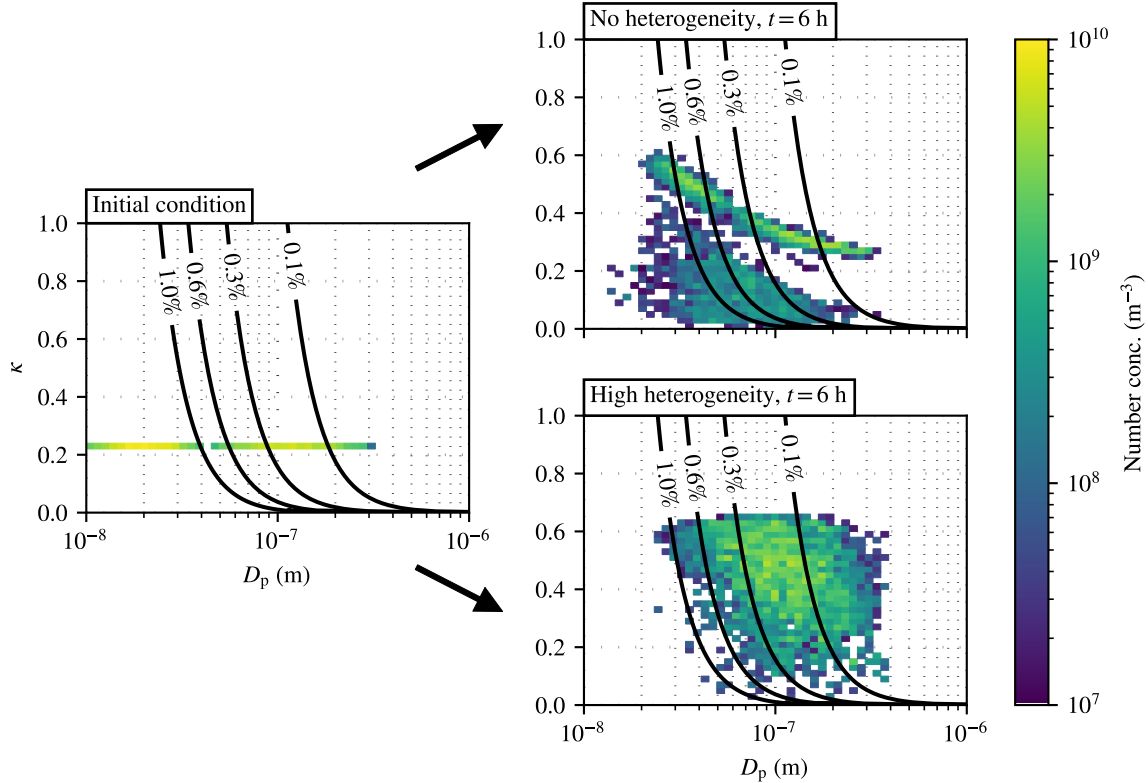


Figure 8. 2-dimensional number distributions $n(D_p, \kappa)$ for emissions scenario extremes. The initial condition is shown on the left, indicating that all aerosol begin as internally mixed particles with uniform κ . On the right, emissions scenarios with minimum spatial heterogeneity (top, no heterogeneity scenario) and maximum spatial heterogeneity (bottom, the high heterogeneity scenario) are shown after 6 hours. Cell coloring indicates particle number concentration. Black solid contours indicate supersaturation in %. Particles to the right of a contour line activate at the indicated supersaturation.

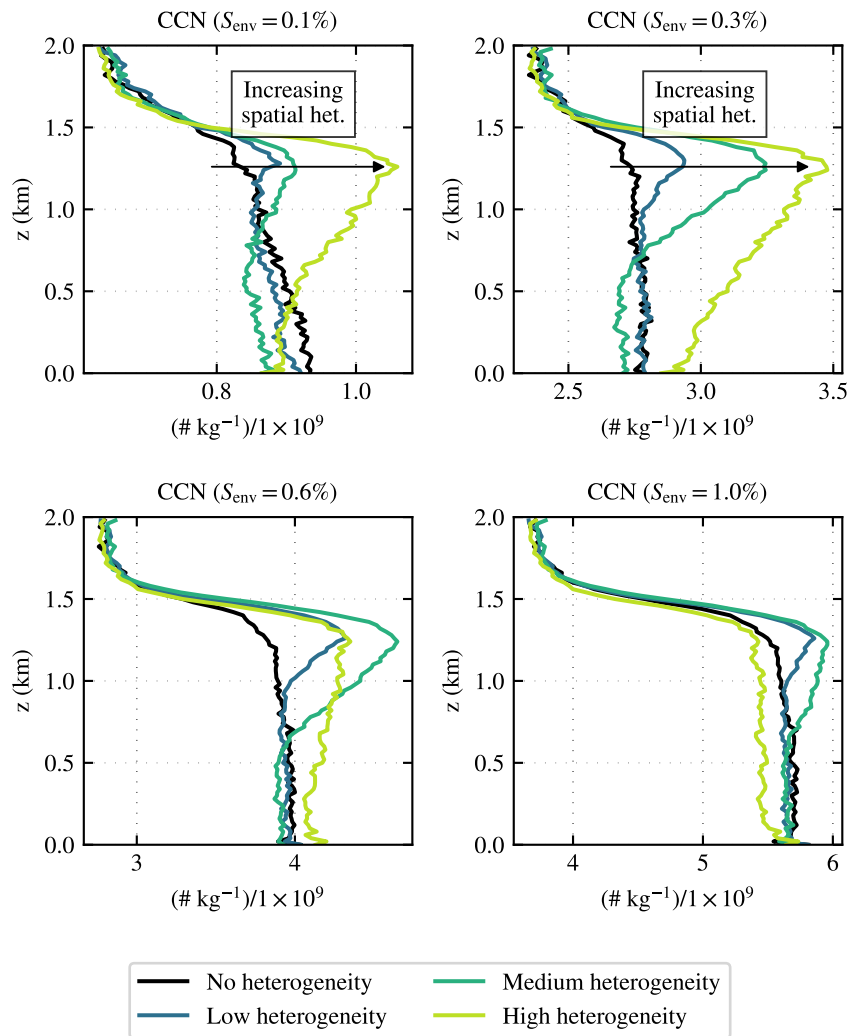


Figure 9. Vertical profiles for CCN concentrations activating at supersaturations $S_{\text{env}} = 0.1, 0.3, 0.6, 1.0\%$ and at $t = 6$ h. Concentrations are displayed in number of CCN per kilogram of dry air and are scaled by a factor of $1 \cdot 10^{-9}$. Values for the no heterogeneity scenario are shown as a solid black line while emissions scenarios 1–3 are shown as colored solid lines.

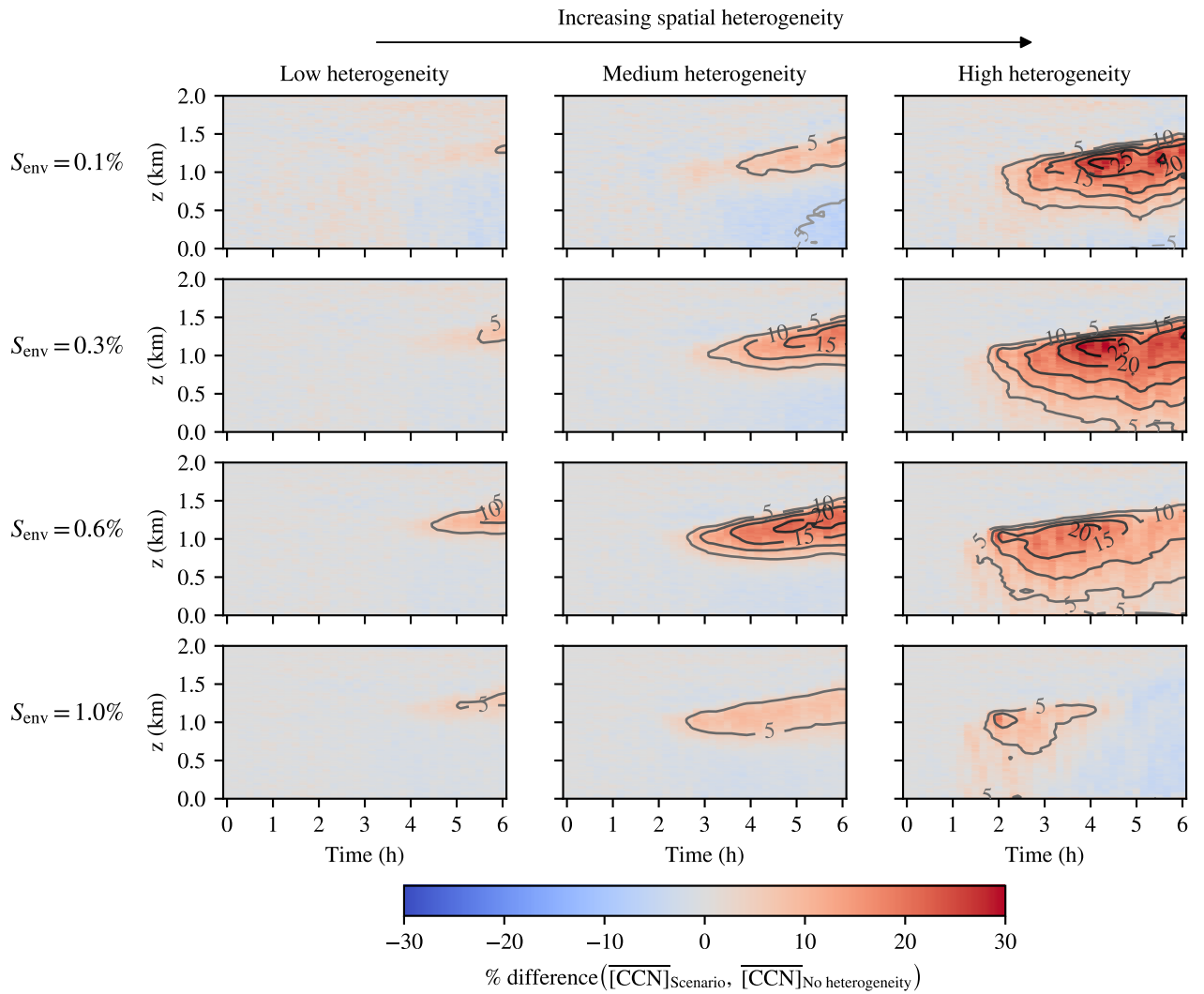


Figure 10. Time-height plots for the percent difference between CCN concentrations in the no heterogeneity scenario and each emissions scenario and supersaturation level. Scenarios are organized by column. The supersaturation of CCN activation is organized by row. Red indicates an increase in CCN relative to the base case while blue indicates a reduction in CCN concentrations. Contour lines indicating regions of constant percent difference are drawn on each panel in increments of 5%.

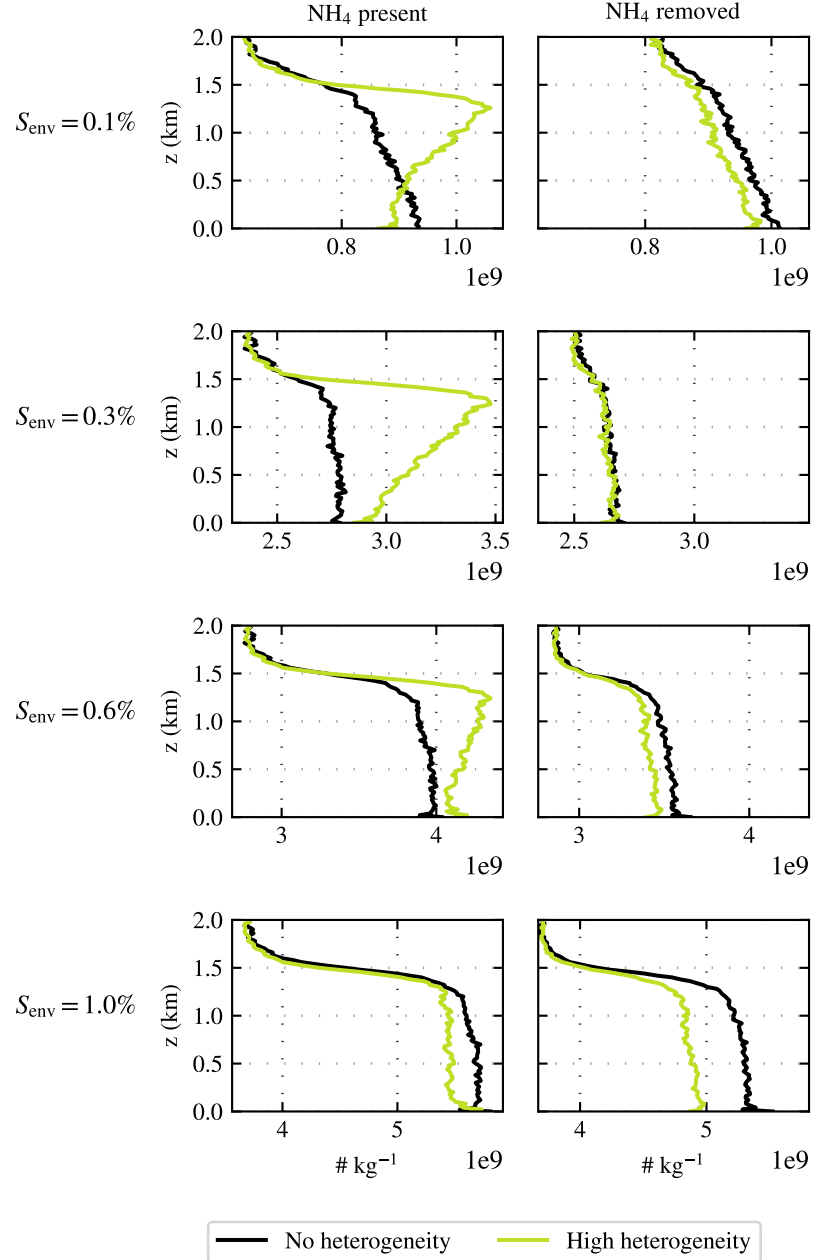


Figure 11. Vertical profiles for CCN concentrations in ammonia-free simulations that activate at supersaturations $S_{\text{env}} = 0.1, 0.3, 0.6, 1.0\%$ and at $t = 6$ h. Concentrations are displayed in number of CCN per kilogram of dry air and are scaled by a factor of $1 \cdot 10^{-9}$. Profiles for scenarios with ammonia are shown as solid lines while scenarios without ammonia are displayed as dashed lines for the no heterogeneity scenario (black) and the high heterogeneity scenario (chartreuse).